PROCEEDINGS, 50th Workshop on Geothermal Reservoir Engineering
Stanford University, Stanford, California, February 10-12, 2025
SGP-TR-229

Fracture characterization revealed by microseismicity at Cape Modern Geothermal Field, Utah

Nori Nakata[1,2], Hilary Chang[2], Sin-Mei Wu[3], Zhengfa Bi[1], Li-Wei Chen[1], Florian Soom[1], Hui Gao[4], Aleksei Titov[5], Sireesh Dadi[5]

[1]Earth and Environmental Sciences Area, Lawrence Berkeley National Laboratory, 1 Cyclotron Rd., Berkeley, CA 94720

[2]Earth, Atmospheric and Planetary Sciences, Massachusetts Institute of Technology, Cambridge, MA 02139

[3]Dapartment of Earth Sciences, University of Hawaii at Manoa, Honolulu, HI 96822

[4]School of Earth and Space Sciences, University of Science and Technology of China, Hefei, China

[5]Fervo Energy, Houston, TX 77002

nnakata@lbl.gov

Keywords: enhanced geothermal system, seismic monitoring, fracture, Cape Modern

ABSTRACT

Understanding stress and strain states in geothermal reservoirs is critical for mitigating induced seismicity and optimizing reservoir management, particularly in enhanced geothermal systems (EGS). This study investigates seismicity and subsurface fracture characterization at the Cape Modern Geothermal Field, Utah, leveraging a diverse array of seismic sensors, including background seismometers, surface nodal networks, and borehole distributed acoustic sensing (DAS). By integrating automatic earthquake detection, image processing, and stress drop analysis, we characterize both large and small fracture structures that influence seismic behavior.

We develop a multi-stage workflow to reconstruct fault surfaces from discrete earthquake hypocenters, employing Gaussian kernel transformations, fault orientation scanning, and surface voting methods to enhance structural continuity. Additionally, we estimate earthquake stress drops using DAS data to infer small-scale fracture properties and fluid pathways. Our analysis reveals stress drop variations between 1–20 MPa and depth-dependent attenuation effects, with implications for seismic hazard assessment and permeability evolution. These findings enhance our understanding of the stress state in geothermal reservoirs and provide insights into fault mechanics and induced seismicity.

1. INTRODUCTION AND DATA

Understanding the detailed stress and strain states in the reservoir and surrounding structure is crucial for mitigating large induced seismicity and reservoir management in geothermal fields. This is especially important when we increase the usage of geothermal resources and employ enhanced geothermal systems (EGS). We consider that there are two key factors to characterize subsurface stresses; densification of seismic monitoring sensors and fracture characterization. We have deployed multiple types of sensors at the Cape Modern Geothermal Field, Utah, to monitor seismicity including background seismometers, dense surface nodal network and borehole distributed acoustic sensing (DAS). Different types of sensors have their own sensitivities, and using them is important to observe and characterize wide aspects of seismicity. Then we apply image processing and earthquake source characterization to identify large- and small-scale fractures.

Six seismic monitoring stations were installed at the Cape Modern site aimed at complementing the extensive, preexisting monitoring network of the University of Utah Seismograph Stations, in collaboration with the Utah FORGE site (Figure 1). Five of the sensors are installed in shallow (~40 m deep) boreholes, and the other is installed in a ~1 m deep posthole. All six sensors are 3-component, low-noise optical accelerometers manufactured by Silicon Audio and ASIR Seismic, who package the downhole sondes. They have a nominal sensitivity of 60 V/g, a dynamic range of 172 dB, and a passband from 0.005 to 1500 Hz (per manufacturer specifications; Hopp et al., 2022). Data from these stations are streamed to the EarthScope DMC in real time over the cell network and are archived under the network code 6K.

In addition to the background seismometers, we deploy 500 surface nodal sensors and 480 single-component geophones with real-time telemetry system (Figure 1). The surface nodes are SmartSolo IGU-16HR with 5Hz sensors, which is three components with 30 days of battery. For most of locations, we deploy two IGUs, and one of them has delayed starting time to reduce the frequency of field work. We also deploy borehole DAS in the Cape Delano1OB well and Utah FORGE 16B well. Each cable has approximately 1500 sensors with 2-m spacing. There is also surface DAS, but we do not use these data for our processing in this study. Both the surface nodes and DAS provide continuous seismic data and monitor seismicity seamlessly.

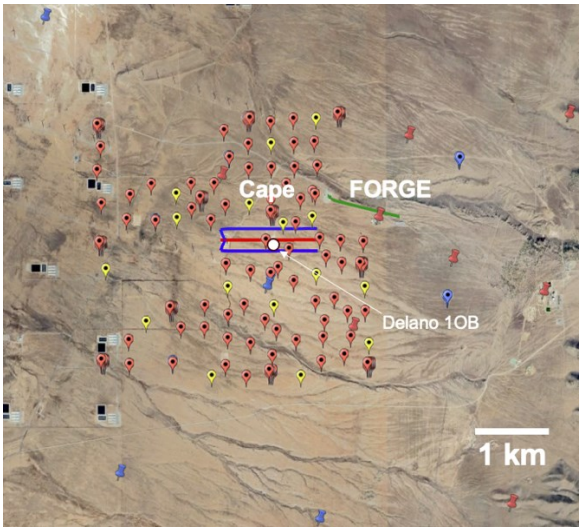

Figure 1: The site map of the Cape Modern and Utah FORGE geothermal fields at Milford, Utah. The push pins are background seismometers and the circular pins indicate the location of surface nodal stations. The white circle is the location of the vertical well, which is instrumented by DAS.

2. SEISMICITY

LBNL has set up an automatic processing system of seismicity using the background seismic network using seiscomp, and then refine the automatically processed earthquake catalog using other datasets. The seismic data processing pipeline for the LBNL seiscomp server comprises the following parts:

1. Data telemetry over the cellular network using the RTPD and seedlink protocols
2. Initial detection is conducted using a short-term average/long-term average (STA/LTA) detection algorithm. The detection statistic is calculated on vertical component data bandpass filtered between 3 and 30 Hz with a short-term window of 0.1 seconds and a long-term window of 5 seconds. When the short-term/long-term ratio exceeds 3, a detection is triggered. The detection is turned off once the ratio falls below 1.5.
3. Once a detection is triggered, seiscomp launches both a P and S-phase post-picking algorithm to refine the arrival times. Both of these algorithms are based on the Akaike Information Criterion (AIC).
4. All phase picks made by steps 2 and 3 are fed to a phase association algorithm. The phase association is a cluster search based on the DBSCAN algorithm whereby P-picks are continually clustered and associated. The clustering metric is the vector sum of the time difference between any pair of picks and the travel time between the stations corresponding to these picks (assuming some average crustal velocity). Once a cluster of P-picks has been formed, additional picks can be associated to this origin from later picks and other origins.
5. Each final origin created in step 4 is then relocated using a linearized location algorithm with a 1D velocity model tailored to the region in which the picks were made.
6. If an initial location falls within a set of predefined regions (within 25 km of the Cape site, for example), the origin is then relocated using the NonLinLoc software package with a 3D velocity model.
7. Two types of magnitudes are estimated for the Cape site: local magnitude (Ml) and duration magnitude (Md). For each pick made, an Ml and Md station magnitude is estimated (Ml being amplitude-based and Md being based on the duration of the event waveform). Ml amplitudes are calculated as the absolute maximum amplitude on 3-Hz highpassed horizontal waveforms after simulation of a Wood-Anderson response. Md amplitudes are using the parameters estimated for Utah by Pechmann et al., 2006. The network magnitude for each type is computed as the average of all station magnitudes, ignoring outliers beyond the upper and lower 12.5 percentile. Until December 2024, due to difficulties in processing data across multiple fields with different magnitude reporting requirements, we stopped estimating the “summary magnitude”, “M”, which was simply the average of Ml and Md network magnitudes.

An example product of the earthquake catalogs are shown in Figures 2 and 3.

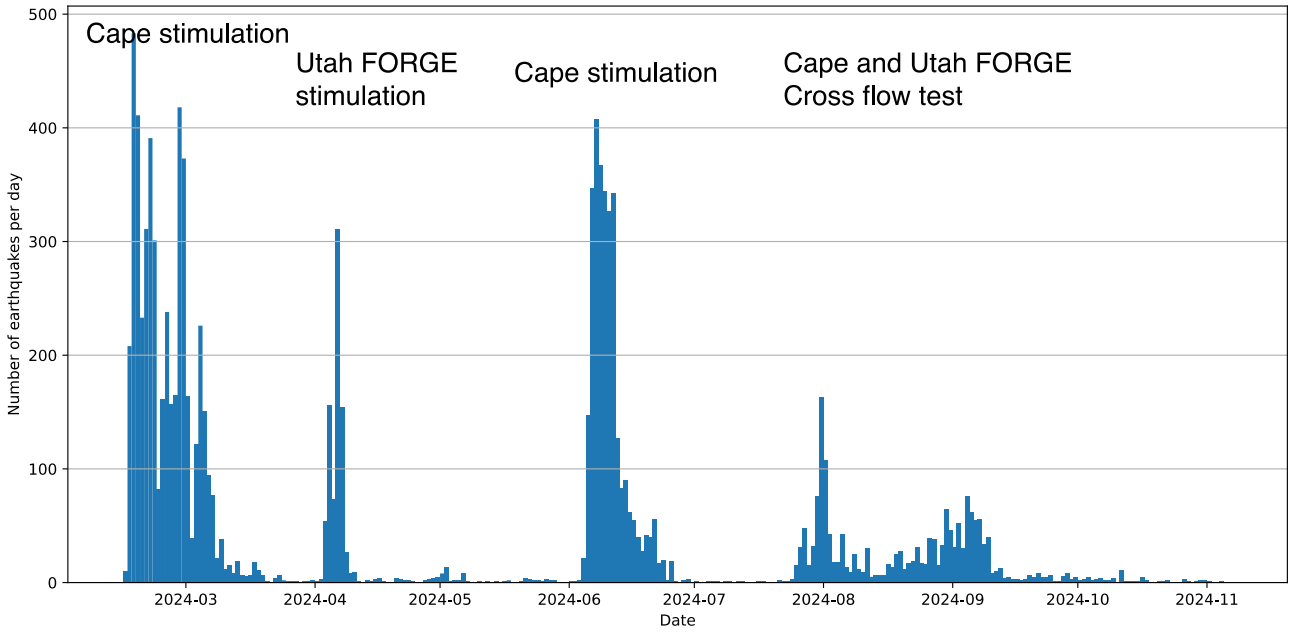

Figure 2: Number of earthquakes in each day (midnight-midnight in UTC). The first, third and fourth high volumes of earthquakes is related to the Cape Modern stimulation and the second one is to the Utah FORGE. With template matching, we detect 8 times more events. The text shows the rough timing of operations.

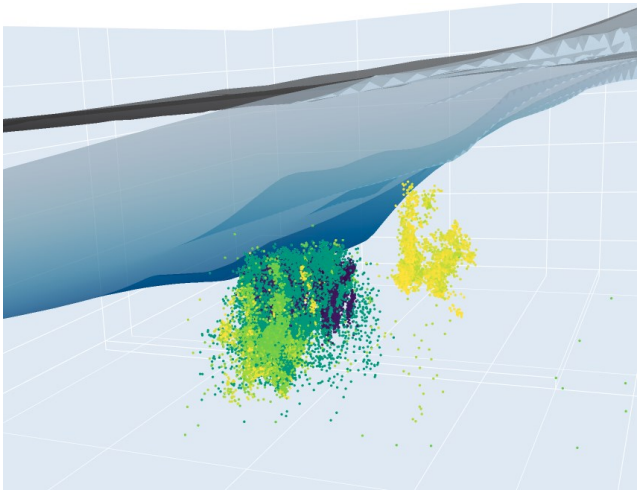

Figure 3: Seismicity locations (each dot) according to the ground surface (gray) and the top of the granite (blue). The dots are colored by the time of events, blue to yellow as February to November, and the left portion (west side) is related to the Cape Modern site and the right portion is for Utah FORGE.

3. LARGE FRACTURE CHARACTERIZATION WITH IMAGE PROCESSING

Understanding fault surfaces and their properties is crucial for seismic hazard assessment and earthquake source physics. However, the representation of earthquake hypocenters as scattered points and the discrete nature of seismic data hinders accurate fault surface reconstruction. To address these issues, we propose a multi-stage workflow for the reconstruction of fault surfaces from earthquake data (Figure 4). Our workflow begins with the transformation of floating, discrete hypocenters into a three-dimensional fault attribute volume. This initial step lays the foundation for subsequent analyses and mitigates data representation limitations.

Then we construct a local isotropic Gaussian kernel to account for the uniform effect of each hypocenter data point in space. Additionally, we introduce a local anisotropic Gaussian kernel to enhance constraint on fault surface orientation. Transforming each hypocenter data point into a local Gaussian volume result in the creation of an initial fault attribute image. To further enhance the representation of fault attributes, we employ the fault orientation scanning method. A local window is established for each grid point, and all possible

combinations of strike and dip directions within this window are systematically scanned and summed. The maximum value among these directions is selected as the new attribute value for the grid point. This iterative process results in a fault orientation scanning image characterized by improved fault attributes.

While the fault orientation scanning method enhances attribute values, it still lacks high-resolution structural details. To address this limitation, we introduce the optimal surface voting method. This technique generates local fault surfaces for grid points with high values and accumulates them to produce a more precise voting score image. Leveraging the accurate voting score image, we employ the surface growth method to reconstruct the final fault surfaces. This step refines the fault representation, providing a detailed and high-resolution view of the fault structures.

The final step in our workflow involves extracting explicit fault surfaces from the optimal surface voting image. This is accomplished through a surface growth method, which initializes surface patches at high-scoring regions, iteratively expands the surfaces by incorporating neighboring points with compatible orientations and high attribute values and smooths and refines the final surfaces to ensure structural continuity and geological plausibility. This results in a reliable reconstruction of the fault network, capturing both primary and subsidiary fault structures with high accuracy.

In conclusion, by addressing data discreteness and enhancing attribute continuity through various stages of processing, our method provides a comprehensive representation of fault structures (Figure 5). This approach holds promise for advancing seismic hazard assessment, contributes to a deeper understanding of seismic source physics, and characterizes possible fluid paths in the reservoir.

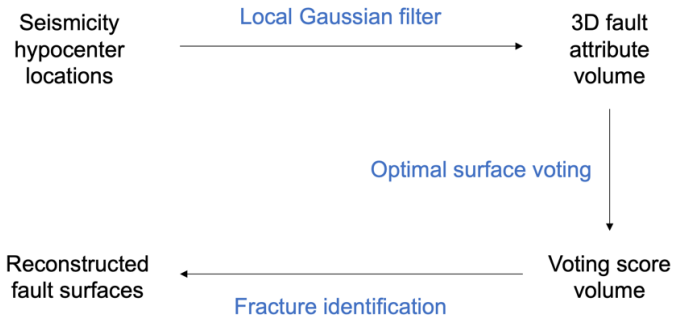

Figure 4: The workflow of image processing for large fracture characterization. Black text indicates the data and blue text the processing.

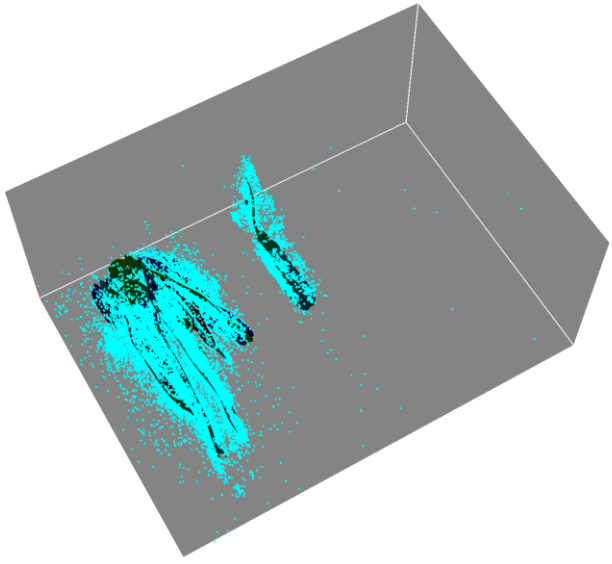

Figure 5: Identified fractures (dark-color planes) and seismicity (light blue dots).

4. SMALL FRACTURE CHARACTERIZATION WITH EARTHQUAKE STRESS DROP ANALYSIS

Stress release during an earthquake is proportional to the slip divided by the length scale of the rupture, and hence we can evaluate the size of the fractures related to seismicity at geothermal fields, and possibly the change of fluid paths and permeability, via earthquake stress drop analysis. It is a basic property of earthquakes fundamental to understanding the physics of the source and its energy budget. The stress release also governs the amplitude of ground motions at the frequencies important for strong ground motion prediction and so is inherent to seismic hazard analysis. Since the pioneering work of Brune (1970) innumerable studies have attempted to use a relatively simple spectral method to estimate the source dimension and stress drop of small and moderate earthquakes in multiple settings (for example, Abercrombie 1995, Shearer et al., 2006, Huang et al., 2017, Boyd et al., 2017, and references therein). The goals of such studies have been to characterize the source process by estimating the spatial extent of slip and average stress drop. Together with the seismic moment, these parameters define the earthquake energy budget (Kanamori and Brodsky, 2004), and also the expected ground motions at frequencies of engineering interest (>1 Hz, Cotton et al., 2013, Trugman and Shearer, 2018). Different analyses have focused on determining whether earthquake sources are scale invariant (e.g. Abercrombie 1995, Abercombie, 2013; Trugman and Shearer 2017), probing the energy budget (e,g. Abercrombie and Rice, 2005) and resolving whether the source process is controlled by factors such as temperature, strain rate, depth, or anthropogenic inducing (e.g. Viegas et al., 2010, Allmann and Shearer, 2007; Sumy et al., 2017; Boyd et al., 2017, Huang et al., 2017, Trugman et al., 2017; Zhang et al., 2016). To characterize earthquakes, we focus on the DAS data in the vertical well Delano 1OB and the events that occurred during stimulations between February 23 and March 14, 2024 (Figure 6). The DAS channel spacing is 2 m and the sampling rate is 1000 Hz.

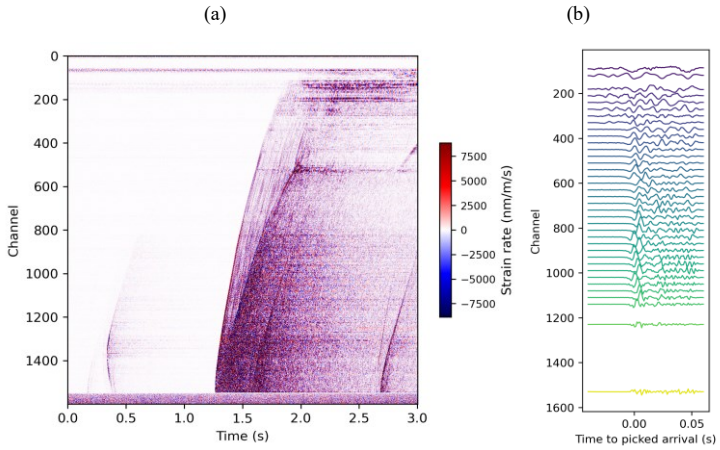

Figure 6: A microearthquake event (ML=1.3) during stimulation. (a) The wavefield is captured by the fiber along well 1OB. (b) P arrivals that are aligned by the picked arrival time.

4.1 Attenuation analysis

The observed earthquake spectra combine both the source, path, and site effects. To separate the path and site effects from the source, we need to analyze the attenuation structure (Chang et al., 2024). We select a few events located at the end of the well 1OB (Figure 6a). For each event, we use a kurtosis picker (Beyreuther et al., 2010) to pick the P arrival time and cut the waveform between -0.05 and 0.05 s around the arrival time (Figure 6b). We demean, detrend, taper both ends, and calculate the Fourier spectra. To enhance the signal-to-noise ratio (SNR), we stack the spectra every 10 m (5 traces in each stack as the DAS channel separation is 2 m). Then, we divide the stack spectra of the P arrival between channels separated by 160 m. The resulting deconvolved spectra contain the wave propagation effect along the wellbore. The P-wave spectra at shallower depth experience higher spectra decay between 20 – 200 Hz associated with higher attenuation.

We estimate the Quality Factor (Q) by fitting the deconvolved spectra between 20 and 200 Hz based on the travel time of waves between channels (Figure 7). The Q increases gradually from 20 to 200 between 200 m and 1500 m depth due to sediment compaction. The sediment-granite interface is likely between 1400 - 1700 m depth. Below the granite basement, the Q ranges between 50 – 700 without a clear trend. We will use the Q information in the source parameter analysis.

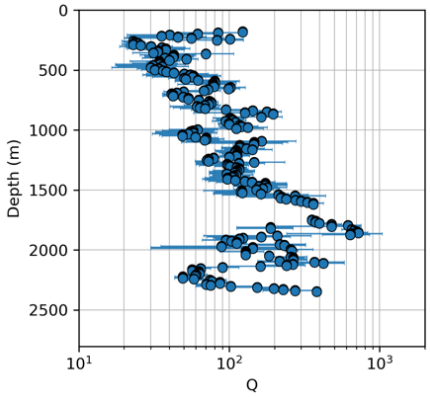

Figure 7: Quality factor (Q) estimated by deconvolved P-wave spectra of four microearthquake events (ML=1.2 –1.5) that are located near the bottom of well 1OB. The circles are the median of four events and the error bars indicate one standard deviation.

4.2 Source parameter analysis

We consider modeling earthquake single spectra in this analysis. We focus on 83 events that occur between February 23 – March 14 with good quality picked arrival times using the kurtosis picker. We first convert the strain rate data of P arrivals (-0.05 – 0.05 s around the picked P arrival times) to displacement. Following Wang et al. (2018), we integrate the time series of P arrivals twice in time and multiply the data by the apparent velocity, estimated by the picked arrival time and the distance between channels. We only use channel numbers from 800 to 1000 where the SNR is consistent among events.

We calculate the Fourier displacement spectra and resample the spectra to have equal sample spacing in the frequency domain. Then, we perform a point-wise quality control to discard spectral data points with SNR less than 9. We stack channels every 20 m (5 channels in one stack). We use a least-square approach to fit the spectral model Ω_R to the stacked displacement spectra (**Error! Reference source not found.**). In the spectral model, we use the median Q_{site} estimated in the attenuation analysis for each stack and assume t_{site} is 10% of the total travel time. We fix $n = 2$ to prevent parameter trade-offs (Kaneko and Shearer, 2015; Chang et al., 2025) and use the Boatwright model ($\gamma = 2$; Boatwright, 1978). The dependent parameters are f_c , Q_{path}, and Ω_0.

The source radiuses estimated by the corner frequencies are between 3 and 20 m (**Error! Reference source not found.**). The moment magnitudes estimated by DAS positively correlate with the local magnitudes estimated by surface stations, suggesting the potential of DAS for characterizing the event magnitude (Figure 8).

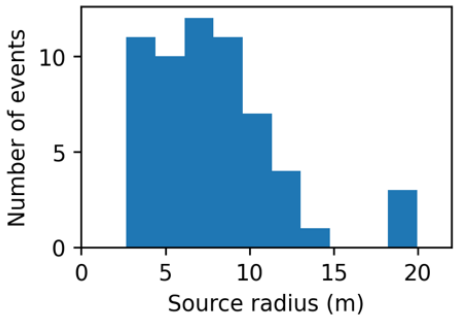

Figure 8: Median source radius (a) estimated by corner frequencies from the stacked displacement spectra.

The majority of the events we analyze have stress drops ($\Delta\sigma$) between 1 and 20 MPa (Figure 9a) and path-dependent attenuations (Q_{path}) of 100 – 3000. The lowest magnitude that we can resolve all source parameters is approximately -1.0, restricted by the upper bandwidth limit (~380 Hz). Q_{path} increases with increasing source depth, which agrees with expectation. The apparent stress drops are larger for events with higher Q_{path} in **Error! Reference source not found.**a, which can potentially be due to trade-offs between parameters in the fitting process. To reduce the trade-offs, we try fixing $Q_{path} = 600$ and repeat the fitting process, which results in more concentrated stress drop estimates (between 1 and 10 MPa; Figure 9b).

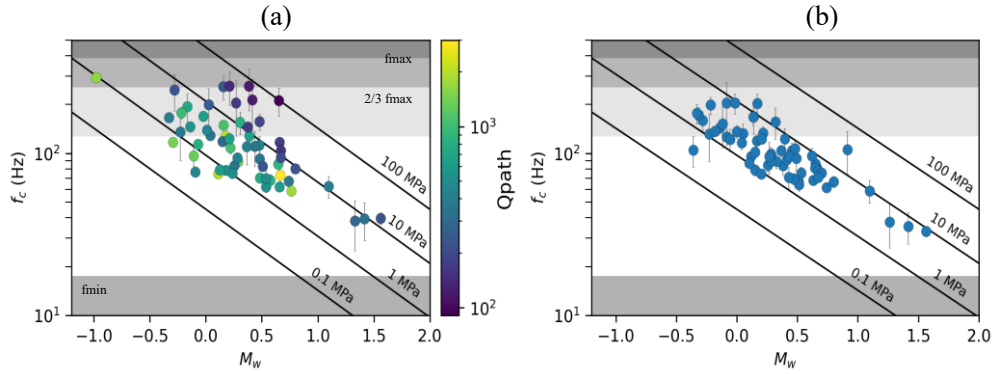

Figure 9: Relation between corner frequency (f_c) and moment magnitude (M_w). The solid lines indicate constant stress drops of 0.1, 1, 10, and 100 MPa. (a) Letting the path-dependent attenuation (Q_path) be a dependent variable. (b) Fixing Q_path at 600. Each dot is the median value of all DAS measurements in well 1OB for an event. The error bars indicate the standard deviation. fmax and fmin are the median maximum and minimum available frequency bandwidth, respectively.

5. CONCLUSIONS

This study provides a comprehensive analysis of seismicity for subsurface fracture characterization at the Cape Modern Geothermal Field, employing a combination of high-resolution seismic monitoring, image processing, and earthquake stress drop analysis. By integrating multiple seismic sensor datasets, we successfully characterize both large- and small-scale fractures that contribute to the stress state and permeability structure of the reservoir.

Our results highlight the effectiveness of advanced image processing techniques in reconstructing fault surfaces, offering improved continuity and resolution over traditional hypocenter-based approaches. The stress drop analysis using DAS data further refines our understanding of small-scale fractures and their role in fluid flow dynamics. The observed correlation between depth-dependent attenuation (Q) and stress drop suggests a complex interplay between lithology, fault mechanics, and fluid interactions in the geothermal reservoir.

These findings have significant implications for seismic hazard assessment and reservoir characterization and management in geothermal energy production. The methodology presented here provides a robust framework for future studies in induced seismicity monitoring and subsurface stress modeling, contributing to the sustainable and safe development of geothermal resources.

6. ACKNOWLEDGEMENTS

We are grateful to Fervo Energy for their collaboration to this work and permission to present the results. This work is supported by the U.S. Department of Energy, Office of Energy Efficiency and Renewable Energy (EERE), Geothermal Technologies Office, under Award Number DE-AC02–05CH11231 with Lawrence Berkeley National Laboratory.

REFERENCES

Abercrombie, R. E. (1995). Earthquake source scaling relationships from− 1 to 5 ML using seismograms recorded at 2.5-km depth. Journal of Geophysical Research: Solid Earth, 100(B12), 24015-24036.

Abercrombie, R. E. (2013), Comparison of direct and coda wave stress drop measurements for the Wells, Nevada, earthquake sequence, J. Geophys. Res., 118, 1458–1470, doi:10.1029/2012JB009638.

Abercrombie, R. E. (2015). Investigating uncertainties in empirical green's function analysis of earthquake source parameters. Journal of Geophysical Research: Solid Earth, 120(6), 4263–4277. https://doi.org/10.1002/2015jb011984

Abercrombie, R. E., and J. R. Rice (2005), Small earthquake scaling revisited: can it constrain slip weakening? Geophys. J. Int., 162, 406-424.

Beyreuther, M., Barsch, R., Krischer, L., Megies, T., Behr, Y., & Wassermann, J. (2010). ObsPy: A Python toolbox for seismology. Seismological Research Letters, 81(3), 530-533.

Boatwright, J. (1978). Detailed spectral analysis of two small New York State earthquakes. Bulletin of the Seismological Society of America, 68(4), 1117-1131

Boore, D. M., & Boatwright, J. (1984). Average body-wave radiation coefficients. Bulletin of the Seismological Society of America, 74(5), 1615-1621.

Chang, H., Nakata, N., Abercrombie, R. E., Dadi, S., & Titov, A. (2024). Toward reliable estimation of source parameters using Distributed Acoustic Sensing for microearthquakes in the Cape Modern geothermal field, Utah. American Geophysical Union 2024 Annual Meeting. Washington, D.C., USA.

Chang, H., Abercrombie, R. E., & Nakata, N. (2025). Importance of considering near-surface attenuation in earthquake source parameter estimation: Insights from Kappa at a dense array in Oklahoma. Bulletin of the Seismological Society of America. https://doi.org/10.1785/0120240137

Cotton, F., R. Archuleta and M. Causse (2013), What is the sigma of the stress drop? Seismol. Res. Letts., 84, 42-48, doi: 10.1785/0220120087.

Eshelby, J. D. (1957). The determination of the elastic field of an ellipsoidal inclusion, and related problems. Proceedings of the royal society of London. Series A. Mathematical and physical sciences, 241(1226), 376-396.

Hanks, T. C., & Kanamori, H. (1979). A moment magnitude scale. Journal of Geophysical Research: Solid Earth, 84(B5), 2348-2350.

Hartzell, S. H. (1978). Earthquake aftershocks as green's functions. Geophysical Research Letters, 5(1), 1–4. https://doi.org/10.1029/gl005i001p00001

Hopp, C., T. Taira, M. Robertson, J. J. Farrugia, C. Layland- Bachmann, and E. Majer (2022). Low- Noise Optical Accelerometers: Bridging the Gaps among Geophones, Accelerometers, and Broadbands in a Deep Borehole, Seismol. Res. Lett. 93, 2367–2376, doi: 10.1785/0220210340.

Huang, Y., W. L. Ellsworth, and G. C. Beroza (2017), Stress drops of induced and tectonic earthquakes in the central United States are indistinguishable, Sci. Adv., 3(8), e1700772, doi: 10.1126/sciadv.1700772.

Hough, S. (1997). Empirical green's function analysis: Taking the next step. Journal of Geophysical Research, 102(B3), 5369–5384. https://doi. org/10.1029/96jb03488

Kaneko, Y., & Shearer, P. M. (2015). Variability of seismic source spectra, estimated stress drop, and radiated energy, derived from cohesive-zone models of symmetrical and asymmetrical circular and elliptical ruptures. Journal of Geophysical Research: Solid Earth, 120(2), 1053-1079.

Madariaga, R. (1976). Dynamics of an expanding circular fault. Bulletin of the Seismological Society of America, 66(3), 639-666.

Pechmann, J. C., J. C. Bernier, S. J. Nava, and F. M. Terra (2006), Correction of systematic time-dependent coda magnitude errors in the Utah and Yellowstone National Park region earthquake catalogs, 1981–2001, Appendix C, in Integrated Regional and Urban Seismic Monitoring—Wasatch Front Area, Utah and Adjacent Intermountain Seismic Belt, edited by W. J. Arabasz et al., Final Tech. Rep., 137 pp., U.S. Geological Survey Cooperative Agreement 04HQAG0014.

Pennington, C. N., Chang, H., Rubinstein, J. L., Abercrombie, R. E., Nakata, N., Uchide, T., & Cochran, E. S. (2022). Quantifying the sensitivity of microearthquake slip inversions to station distribution using a dense nodal array. Bulletin of the Seismological Society of America, 112, 1252–1270. https://doi.org/10.1785/0120210279

Sumy, D. F., Neighbors, C. J., Cochran, E. S., and Keranen, K. M. (2017), Low stress drops observed for aftershocks of the 2011 Mw 5.7 Prague, Oklahoma, earthquake, J. Geophys. Res. Solid Earth, 122, 3813– 3834, doi:10.1002/2016JB013153.

Trugman, D. T., and P. M. Shearer (2017), Application of an improved spectral decomposition method to examine earthquake source scaling in southern California, J. Geophys. Res., doi: 10.1002/2017JB013971.

Trugman, D. T., and P. M. Shearer (2018), Strong correlation between stress drop and peak ground acceleration for recent M 1–4 earthquakes in the San Francisco Bay area, Bull. Seismol. Soc. Am., 108, 929-945, doi: 10.1785/0120170245.

Wang, H. F., Zeng, X., Miller, D. E., Fratta, D., Feigl, K. L., Thurber, C. H., & Mellors, R. J. (2018). Ground motion response to an ML 4.3 earthquake using co-located distributed acoustic sensing and seismometer arrays. Geophysical Journal International, 213(3), 2020-2036.

Zhang, H., D. W. Eaton, G. Li, Y. Liu, and R. M. Harrington (2016), Discriminating induced seismicity from natural earthquakes using moment tensors and source spectra, J. Geophys. Res. Solid Earth, 121, 972–993, doi:10.1002/2015JB012603.